Analysis of the Metal Plate Coupled Resonator With Its Compact In-Line Filter Design Applications

Analysis of the Metal Plate Coupled Resonator With Its Compact In-Line Filter Design Applications

Jiayu Rao, *Member, IEEE*, Cong Sun, Jiajin Lu, Qian Gao, Bowei Zhou, Hualin Zhao, Hai Liu, Sheng Zhang, Povilas Vaitukaitis, *Graduate Student Member, IEEE*, Lei Wang, *Senior Member, IEEE*, and Jiasheng Hong, *Fellow, IEEE*

***Abstract*— This article introduces and analyzes the modified metal plate coupled resonator (MPCR), which can be designed to exhibit distinctive nondegenerate dual-mode characteristics, i.e., having different resonating frequencies and presenting quasi-orthogonal features (e.g., no coupling). By employing different feeding methods, the MPCR can function as either a single-mode or dual-mode resonator, both of which are suited for the design of in-line filters with controllable transmission zeros (TZs). For the single-mode operation, new mixed-coupling-based in-line filters can be designed to yield noteworthy advancements compared to prior research, as these filters achieve arbitrary placement of TZs without necessitating any additional structures. For the dual-mode operation, more compact in-line filters based on transverse coupling topology for achieving quasi-elliptic function response can be designed. In general, all filters developed in this work provide the advantages of adjustable TZs and simple physical configurations. For the rapid prototyping and the experimental demonstration, certain *C*-band filters were designed and manufactured using 3-D metal printing technology. Meanwhile, for the first time, the necessity of introducing post-magnetic tuning is validated and then applied to the mixed-coupled filters. As a result, all testing results showed consistency with the simulated ones.**

***Index Terms*— Bandpass coaxial filter, in-line topology filters, 3-D metal printing, transmission zeros (TZs).**

I. Introduction

MINIATURIZATION and high rejection performance coaxial bandpass filters (BPFs) are urgently needed for adapting to the higher frequency and crowded spectrum demands of the fifth generation (5G) communication systems. For various BPFs, the in-line topology has the simplest physical structures, while transmission zeros (TZs) can enhance the frequency selectivity highly. Hence, recently, in-line coaxial filters with controllable TZs are becoming attractive [1], [2], [3], [4], [5], [6], [7], [8], [9], [10], [11], [12], [13], [14], [15], [16], [17]. In [2] and [3], by placing some of the resonators in different orientations deliberately, the classical cascaded triplet coupling but using in-line topology was achieved. In [4], [5], [6], and [7], in-line filters based on strongly coupled resonator pairs to facilitate TZs were proposed. These in-line topology filters all offered compact sizes and high rejection capabilities. However, a spurious peak at the lower stopband would appear primarily due to the even-mode frequency that is always smaller than the odd-mode one. Another solution is the electrical magnetic mixed coupling, in which a controllable TZ could be generated by controlling electrical magnetic coupling energy ratio between the adjacent resonators [8]. The concept has been extended to effectively design in-line coaxial quasi-elliptic filters, as reported in [9], [10], [11], [12], [13], [14], and [15]. However, in order to independently control the electrical and magnetic energy for adjusting TZs, additional structures, such as the metal rod in [9], [10], [11], and [12], the lumped element capacitor in [13], or the metal strip in [9], are commonly needed in the physical realization of these filters, albeit at the cost of increased losses.

More recently, the waveguide-loaded air slots resonator was proposed in [16] to realize the separation of the resonating electrical magnetic fields, enabling the direct construction of a mixed-coupling dual path for producing a TZ when in-line cascading two resonators. Following this technique, the metal coupled line resonator has been presented to design an in-line filter prototype in our previous report [17], which generated multiple TZs effectively. In this article, a simple modification has been made to the metal plate coupled resonator (MPCR) to allow the provision of dual-mode operation in addition to single mode. Compared with [17], we will show that the single-mode operation of MPCR can also be used to design in-line mixed-coupling filters with controllable TZs and higher quality factor (Q_u) values. Furthermore, by altering the feeding method, the dual-mode MPCR (DM-MPCR) can be excited and employed to design in-line filters as well, yielding adjustable TZs while reducing the overall volume by half. Meanwhile, inspired by the "box section" topology scheme, which is often used in the design of in-line waveguide filters [30], [31], this article will demonstrate that this scheme

Manuscript received 1 November 2023; revised 28 December 2023; accepted 8 February 2024. This work was supported in part by the Chun Hui Program of the Ministry of Education of China under Grant HZKY20220147, in part by the Natural Science Foundation of Jiangsu Higher Education Institutions of China under Grant 23KJB510004, and in part by the Changzhou Science and Technology Program under Grant CJ20235042. *(Corresponding author: Jiayu Rao.)*

Jiayu Rao, Cong Sun, Jiajin Lu, and Qian Gao are with the School of Electrical and Information Engineering, Jiangsu University of Technology, Changzhou 213001, China (e-mail: raojiayu@jstu.edu.cn).

Bowei Zhou and Hualin Zhao are with the High-Tech Research Institute of Nanjing University, Changzhou 213164, China.

Hai Liu and Sheng Zhang are with the School of Information and Control Engineering, China University of Mining and Technology, Xuzhou 221000, China.

Povilas Vaitukaitis, Lei Wang, and Jiasheng Hong are with the Institute of Sensors Signals and Systems, Heriot-Watt University, EH14 4AS Edinburgh, U.K.

Color versions of one or more figures in this article are available at https://doi.org/10.1109/TMTT.2024.3366759.

Digital Object Identifier 10.1109/TMTT.2024.3366759

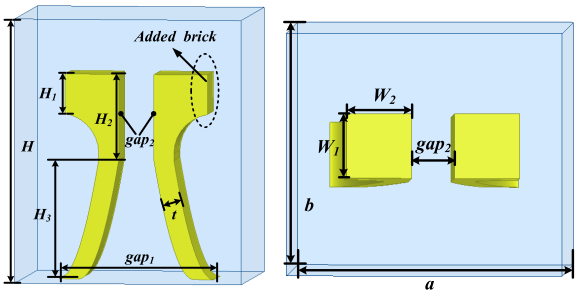

Fig. 1. Layouts of the modified MPCR. Dimensions (unit: mm): $a = 17$, $b = 15$, $H = 20$, $H_1 = 3.5$, $H_2 = 5.5$, $H_3 = 10$, $\text{gap}_1 = 10$, $\text{gap}_2 = 2$, $t = 1.5$, $W_1 = 4$, and $W_2 = 4.3$.

is also available for coaxial BPF applications. Specifically, through cascading DM-MPCR with the two outer conventional coaxial resonators (CCRs), one TZ could be generated at either side of the passband. In addition, as an improvement, cross coupling was introduced for obtaining one more TZ. A total of six 4th-order in-line filters based on different topologies are designed in this article. Compared with published works, all designed filters in this work achieved compact sizes, simple structures, and controllable TZs.

In general, the proposed modified MPCR is analyzed in detail, as presented in Section II, demonstrating its advantages in designing high-rejection in-line filters. Sections III and IV give the complete design methodology for single- and dual-mode-based in-line filters, respectively. Section V presents the comprehensive synthesis procedure for the realization of two additional in-line filter designs that are based on the hybrid cascading of two coaxial resonators and a DM-MPCR. For the experimental demonstration, several filters were manufactured by adopting 3-D metal printing technology. To enhance testing accuracy, the post-magnetic-tuning structures, for the first time, are introduced in this work in the context of the mixed-coupling in-line topology filters. The corresponding fabricated filter samples and measured results are given in Sections III–V. The conclusion is given in Section VI.

II. Resonator Analysis

The layouts of the modified MPCR, as illustrated in Fig. 1, comprise an outer metal enclosure ($a \times b \times H$) and an inside metal coupled plate. The metal coupled plate contains the curved part (H_3) as the resonant inductive and the rectangular part (H_2) as the resonant capacitance to achieve the so-called metal plate coupled mode. Compared with [17], the bottom end of the metal coupled plate is not attached to the side wall to achieve higher Q_u. On the other hand, extra metal bricks ($W_1 \times W_2 \times H_1$) are added at open ends to enable adjusting the coaxial mode (CM) frequency flexibly. Note that W_1 is better at less than 7.0 mm to ensure that the structures can be printed while avoiding using supports. Other dimensions of MPCR are metal plate thickness (t), bottom gap, and top gap (gap_1, gap_2).

Fig. 2 gives the E-field and current distribution patterns of DM-MPCR. As shown, the E-field of the metal plate coupled mode mainly resides within the gap between the rectangular parts, while the CM is distributed at the gap between the open ends and the top wall of the outer enclosure. In this

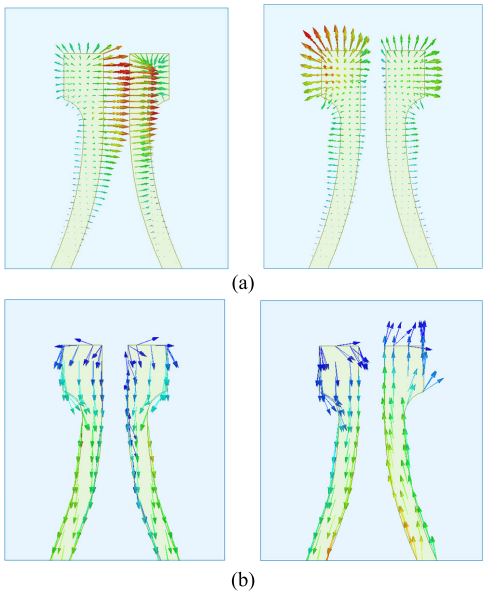

Fig. 2. Fields distribution features of the DM-MPCR. (a) E-field. (b) Current.

regard, the whole metal coupled plate can be seen as the inner conductor of the coaxial resonator. Since E-field orientations of the dual modes are orthogonal, although not entirely so, this allows the DM-MPCR to function as the middle orthogonal dual-mode resonator in the "box section" scheme that will be presented in Section V. Besides, the current distribution of the metal plate coupled mode is odd symmetry about the center gap of the metal coupled plate, which can be characterized as the odd mode. Consequently, the CM corresponds to the even mode. This feature could bring one TZ when both modes were excited, as will be illustrated in Section IV-A. In general, the imperfect E-field orthogonal distribution and the different resonant frequencies of the dual modes enable them like a pair of nondegenerate modes referred to [24].

Fig. 3 gives the simulated metal plate coupled mode and CM frequencies in relationship to two selected critical parameters of the modified MPCR. Unless otherwise stated, the conductivity of the metal in this article is assumed to be $\sigma = 5.8 \times 10^7$ S/m. Other dimensions are listed in Fig. 1. As presented, by increasing the gap_2, the metal plate coupled mode would shift to higher frequencies gradually, while the CM is almost unchanged. This behavior can be attributed to the resonant capacitance of metal plate coupled mode strongly depending on the gap_2 according to the principles of the parallel plate capacitor. Meanwhile, W_1 has a larger impact on CM as the added metal bricks can be regarded as the loaded capacitive cap of the coaxial resonator. In general, the modified MPCR allows either mode to be the fundamental mode. For instance, when gap_2 is less than 2.4 mm, the metal plate coupled mode frequency is lower than the CM and thus will be the fundamental mode. Other related parameters, such as H_1 and gap_1, can similarly be used to manipulate the frequency of each mode. In addition, Q_u of the CM is always much higher than the metal plate coupled mode. This is because the field distributions of the metal plate coupled mode are more concentrated around the metal plate, which leads to smaller surfaces being involved than the CM.

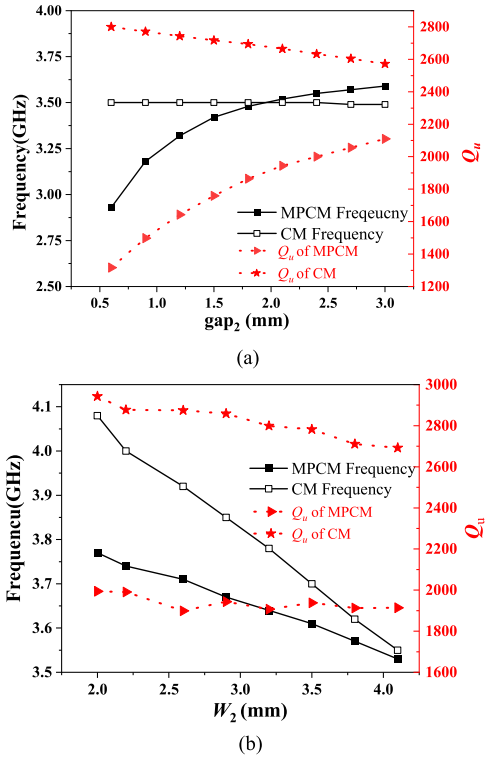

Fig. 3. Simulated CM and metal-plated coupled mode (MPCM) frequencies and Q_u versus the dimensions of (a) gap$_2$ and (b) W_2.

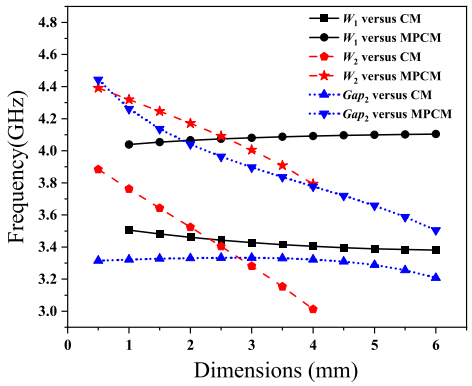

Fig. 4. Simulated CM and MPCM frequencies versus the dimensions of the noncurved MPCR.

It is also interesting to investigate what the situation would be if the metal coupled plates were not made to be curved, as is typically the case with rectangular metal plates. Hence, Fig. 4 gives simulated curves between W_1, W_2, gap$_2$, and associated frequencies. As shown, although altering different parameters within a large range, there is always a frequency gap between the dual modes, that is, the CM frequencies would be consistently lower than the metal plate coupled mode ones. This phenomenon also accounts for the inevitable occurrence of parasitic peaks in the design of strongly coupled resonator filters in [4], [5], [6], and [7]. Table I compares the proposed resonator with a CCR in terms of the volume, Q_u, and f_0. As shown, with the given volume and center frequency, although Q_u of the CM is lower than the CCR, considering that the MPCR can use single/dual modes to design in-line filters without needing extra parts, the spatial utilization remains competitive.

TABLE I
COMPARISON OF THE CCR AND THE PROPOSED RESONATOR

	Volume (mm^3)	Q_u	f_0 (GHz)
CCR	17 × 15 × 20	3262	3.50
MPCR	17 × 15 × 20	CM: 2853	CM: 3.50
		MPCM: 1906	MPCM: 3.51

CM: Coaxial Mode. MPCM: Metal Plated Coupled Mode.

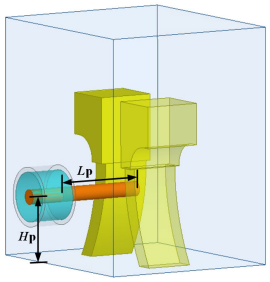

Fig. 5. 3-D side view of capacitive feeding for single mode excitation.

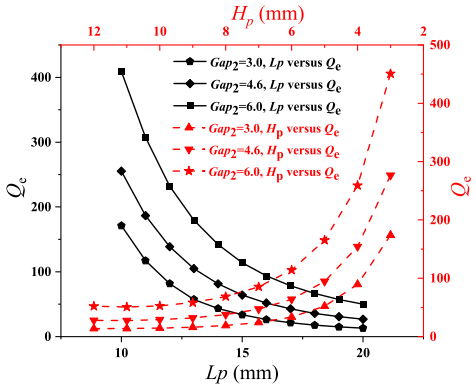

Fig. 6. Simulated Q_e versus L_p and H_p with different gap$_2$.

III. IN-LINE FILTER DESIGN BASED ON THE CM

The above analysis has shown that the CM has higher Q_u values than the metal plate coupled mode. Hence, compared with [17], the CM would be used to design higher performance in-line filters in this work. We would prove that the CM is also available for achieving internal electrical–magnetic mixed coupling as the metal plate coupled mode.

A. External Coupling

The indirect (capacitive) input–output 50-Ω coaxial cables are utilized to feed the single-mode coaxial resonator, as illustrated in Fig. 5. Both the height (H_p) and the length of the feed probe (L_p) can adjust the external coupling (Q_e) strength. The required Q_e can be extracted using the following equation [18]:

$$Q_e = \frac{\omega_0 \tau_{\max}}{4} \tag{1}$$

where ω_0 represents the resonant angular frequency, whereas $\tau_{\max}$ is the maximum group delay of S_{11}, which occurs at resonance. Fig. 6 gives the extracted Q_e values concerning

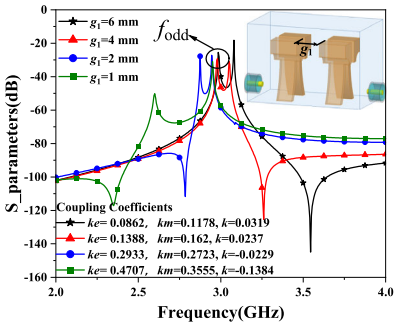

Fig. 7. Simulated S_{12} and related coupling coefficients of the 2nd-order filter versus different g_1.

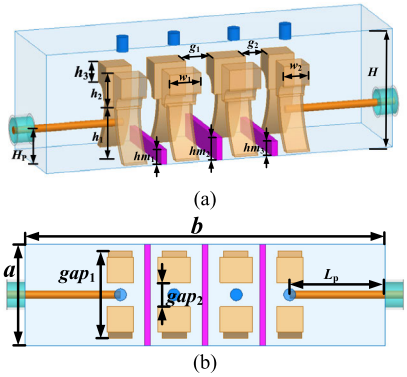

Fig. 8. Common layouts of the 4th-order CM in-line filters. (a) Side-front view. (b) Top view. Dimensions (unit: mm). Filter I: $a = 17.00$, $b = 60.00$, $H = 20.00$, $h_1 = 8.50$, $h_2 = 5.90$, $h_3 = 3.50$, $g_1 = 4.98$, $g_2 = 4.02$, $w_1 = 5.39$, $w_2 = 4.40$, $H_p = 5.50$, $L_p = 15.90$, $\text{gap}_1 = 14.60$, and $\text{gap}_2 = 4.00$. Filter II: $a = 17.00$, $b = 60.00$, $H = 20.00$, $h_1 = 8.07$, $h_2 = 5.57$, $h_3 = 3.50$, $g_1 = 1.46$, $g_2 = 3.12$, $w_1 = 6.25$, $w_2 = 4.80$, $H_p = 6$, $L_p = 16.00$, $\text{gap}_1 = 12.20$, and $\text{gap}_2 = 4.60$.

both H_p and L_p that the effective control can be observed with different gap_2. It should also be noted that a larger gap_2 will get a larger Q_e with the same H_p and L_p.

B. Inner Mixed Coupling

To confirm that the CM of MPCR is capable of featuring the mixed-coupling characteristics without needing to introduce extra structures, the 2nd-order filter with weak capacitive feeding is simulated, as shown in Fig. 7. The weak feeding can be fulfilled by taking a very short probe (smaller than 0.5 mm). All physical dimensions are detailed in Fig. 1, except for the adjustable parameter of g_1. The corresponding curves are also plotted in Fig. 7, where two resonant peaks f_1 and f_2 ($f_1 < f_2$) and one TZ can be seen clearly. The electrical (k_e), magnetic (k_m), and normalized coupling coefficient (k) can be obtained using the following equations:

$$k_e = \frac{f_z^2}{2 \cdot f_0^2}\left(\frac{f_0^2 - f_{\text{odd}}^2}{f_z^2 - f_{\text{odd}}^2} + \frac{f_0^2 - f_{\text{even}}^2}{f_{\text{even}}^2 - f_z^2}\right) \tag{2}$$

$$k_m = \frac{1}{2}\left(\frac{f_{\text{odd}}^2 - f_0^2}{f_{\text{odd}}^2 - f_z^2} + \frac{f_{\text{even}}^2 - f_0^2}{f_z^2 - f_{\text{even}}^2}\right) \tag{3}$$

$$k = \frac{k_m - k_e}{1 - k_m \cdot k_e} \tag{4}$$

where f_z is the TZ point and f_0 is the extreme point between f_{even} and f_{odd} at the maximum group delay of S_{11}. In addition, when TZ appears below the passband, f_{even} is f_1. Conversely, when TZ appears above the passband, f_{even} is f_2. As can be seen, the larger g_1 will get a larger inductive coupling, which leads to TZ appearing at the upper side of the passband. Conversely, the TZ would be shifted to another side of the passband by decreasing g_1. This is because the mixed coupling turned into the capacitive-dominant coupling. In general, the simulated results indicate that by solely changing the distance between the adjacent resonators, the coaxial-mode-based filter could attain the required mixed coupling, which is equal to the dual-path coupling structures described in [9], [10], [11], [12], [13], [14], and [15].

C. Fourth-Order Filter Realization

Two filters, denoted by filters I and II, with the same f_0 of 3.5 GHz, bandwidth (BW) of 160 MHz and a return loss (RL) of 20 dB were designed based on CM for validation. The common layouts are depicted in Fig. 8, wherein the blue

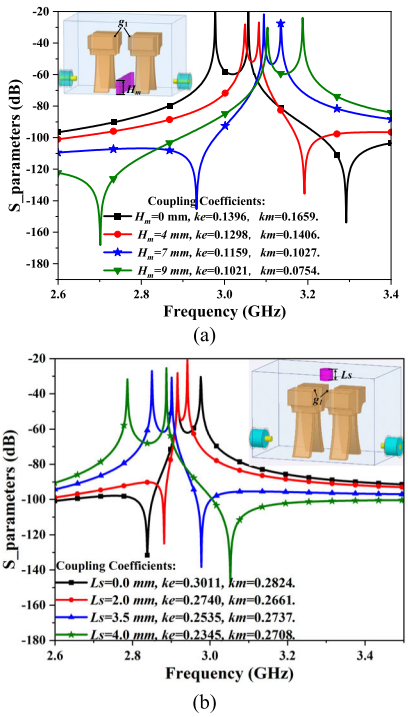

Fig. 9. Simulated S_{12} and related coupling coefficients of the 2nd-order filter versus different. (a) h_m. (b) L_s.

cylinders are frequency-tuning screws. In addition, for the bandwidth tuning, except for the conventional metal screw electric tuning process, we also introduced a magnetic tuning process for the mixed-coupling topology filters, which has never been reported before. The metal septa were applied to replace the screws here, denoted as the purple color. It is imperative to emphasize that the metal septa are intentionally designed to be mechanically adjustable in both upward and downward directions.

To validate the necessity of introducing magnetic tuning as the electric tuning process for the mixed-coupling filters, Fig. 9 gives the simulated curves. As can be seen, increasing the length of L_s, k_e decreased gradually, whereas k_m remained

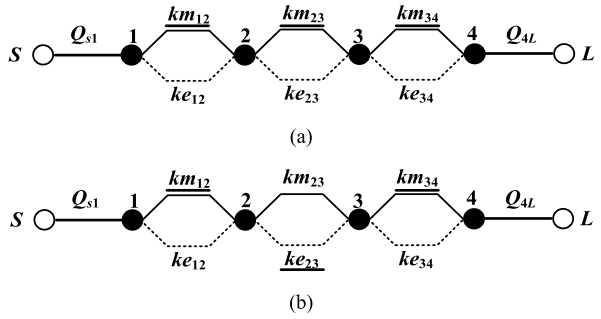

Fig. 10. Topology of the two designed coaxial-mode-based in-line filters. (a) Filter I. (b) Filter II.

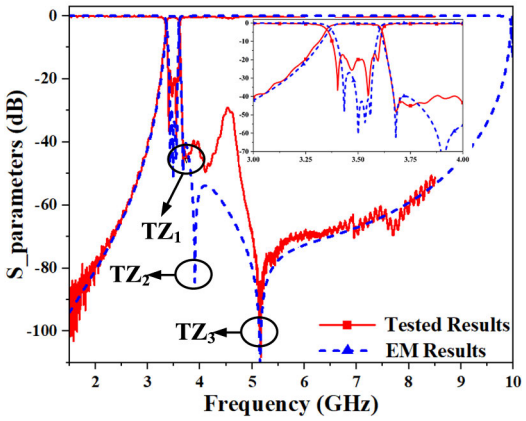

Fig. 11. Simulated and measured S-parameters of filter I.

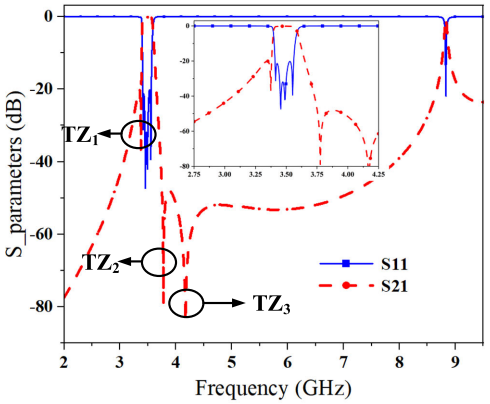

Fig. 12. Simulated S-parameters of filter II.

almost unchanged. Hence, the TZ is shifted from the left to the right side of the passband. Meanwhile, increasing H_m of the metal septa, k_m decreased gradually, while k_e changed a little. The TZ is shifted from the right to the left. Hence, it could be concluded that electrical tuning is only valid for electrical-dominant coupling, while magnetic tuning is for magnetic-dominant coupling. It should also be mentioned that compared to the traditional screw tuning process, metal septa can achieve an extensive adjusting range, as demonstrated in Fig. 9.

In filter design, to improve frequency selectivity performance, filter I incorporates two TZs located at 3.67 and 3.88 GHz. The topology of filter I is depicted in Fig. 10(a), where *S*/*L* indicates the input–output port, and each node is a resonator. The underline denotes the dominant coupling, with all couplings being inductive-dominant to achieve asymmetrical TZs. Based on the filter specifications and mixed-coupling theory in [8], the mixed-coupling coefficients for filter I can be calculated as

$$ke_{(1,2)} = k_{e(3,4)} = 0.1765; \quad k_{m(1,2)} = k_{m(3,4)} = 0.2185$$
$$k_{m(2,3)} = 0.1509; \quad k_{e(2,3)} = 0.1164$$
$$Q_{s1} = Q_{4L} = 13.7253.$$

In the physical realization of the filter, the required mixed-coupling coefficients can be obtained directly by adjusting the distance between the adjacent resonators (g_1 and g_2) or the width of the added brick (w_1 and w_2). Either way eliminates the need for extra structures to independently control electric/magnetic coupling strength. By using (2)–(4) and the optimization algorithm of the covariance matrix adaptation (CMA) evolution strategy embedded in CST Studio Suite 2021 (CST), the dimensions can be determined, as presented in Fig. 8. The simulated responses are plotted in Fig. 11, where three TZs are observed at the upper side of the passband. Among these, TZ_1 and TZ_2 resulted from the mixed couping of $k_{(1,2)}$ and $k_{(2,3)}$, respectively. TZ_3 is generated by the mixed coupling of $k_{(1,3)}$ or $k_{(2,4)}$, which we choose not to manipulate. Overall, the filter exhibits a wide stopband performance with rejection greater than 20 dB from 3.63 to 9.78 GHz. In addition, the simulated insertion loss (IL) is 0.18 dB, and the corresponding average Q_u across the passband hovers at 2933.

On the other hand, filter II is intended to have a pair of TZs located at 3.38 and 3.77 GHz. Hence, the associated topology is presented in Fig. 10(b), where the inductive-dominant coupling of $k_{(2,3)}$ creates the TZ below the passband. In contrast, the capacitive-dominant coupling of $k_{(1,2)}$ produces the TZ above the passband. The normalized mixed-coupling coefficients were calculated as

$$k_{e(1,2)} = k_{e(3,4)} = 0.5006; \quad k_{m(1,2)} = k_{m(3,4)} = 0.5723$$
$$k_{m(2,3)} = 0.3693; \quad k_{e(2,3)} = 0.4240$$
$$Q_{s1} = Q_{4L} = 18.0691.$$

Using the identical extraction process applied to filter I, the dimensions can also be determined, as presented in Fig. 8. The EM simulated responses are plotted in Fig. 12, where two expected TZs (TZ_1 and TZ_2) are produced effectively. Similarly, TZ_3 is also generated by the mixed coupling of $k_{(1,3)}$ or $k_{(2,4)}$. Hence, filter II features rejections exceeding 20 dB from 3.63 to 8.77 GHz. Moreover, the simulated IL and the average Q_u are 0.25 dB and 2743, respectively.

D. Fabrication and Measurement

For rapid experimental validation, filter I was selected to be manufactured by adopting the commercial 3-D metal printing technology, which has revealed the superiority in prototyping microwave/millimeter-wave components [19], [20], [21], [22], [23] with acceptable tolerance. The laser scanning gap is 90 μm, the scanning speed is 1800 mm/s, the laser power is 350 W, and the layer thickness is 35 μm. In addition, all filters printed in this work adopt the powder of AlSi10Mg-0403

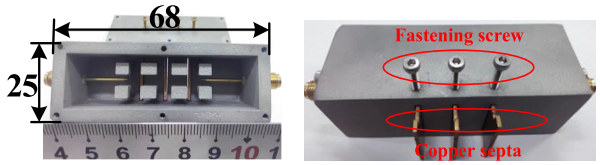

(a) (b)

Fig. 13. Printed samples of (a) filter I. (b) filter V.

with the electrical conductivity $\sigma = 2.56 \times 10^7$ S/m [22]. The printed samples of filter I, as given in Fig. 13(a), were fabricated with only two pieces even in the presence of the inside curved metal plates. The sandblasting process is usually needed to reduce the surface roughness and enhance fatigue resistance. The final measured tolerance for dimensions was within 0.1 mm and the peak roughness is 18 μm. Furthermore, the integrated printing process allowed for a compact outer box, with a mere thickness of 3.5 mm, thus minimizing the overall footprint.

The vector network analyzer (VNA) of Agilent E5071C (100 MHz–8.5 GHz) was used to test radio frequency (RF) responses as plotted in Fig. 11, which agree well with the simulated ones after the post-tuning process. The measured frequency ranges up to 8.5 GHz due to the limitation of the VNA. In detail, the measured f_0 and bandwidth are 3.49 GHz and 183 MHz, respectively. Moreover, the maximum RL approaches approximately 17.5 dB, while the IL is 0.60 dB. The observed discrepancy with simulated ones can primarily be attributed to the rough surface, printing tolerances, and the relatively low conductivity of the powder particles [22]. This could be improved by sliver plating postprocess. Meanwhile, for the tested stopband performance, TZ_2 disappeared, but a minor peak generated. This issue along with larger BW can be attributed to the imperfectly symmetrical placement and length of the feed probe. Nevertheless, the measured results proved that the proposed single mode, i.e., coaxial-mode operation, can result in compact in-line filters with TZ(s).

IV. In-Line Filter Design Based on the DM-MPCR

To achieve further size reduction, the dual-mode operation encompassing one CM and one metal plate coupled mode as discussed in Section II for DM-MPCR was exploited to design in-line filters.

A. Second-Order Filter Design

A 2nd-order filter design is essential since it contains the most critical problems, such as determining the coupling or controlling TZ, which is the basis for higher order filter design applications.

Two 2nd-order filters, filters III and IV, designed with the same center frequency of 3.5 GHz, RL of 20 dB, and 50-MHz bandwidth. Fig. 14 illustrates the common configurations of the proposed 2nd-order filters, made of one single DM-MPCR with 50-Ω coaxial feed. The feeding probe was attached directly to the metal plate to excite the dual modes simultaneously. In addition, filter III was specified to have a TZ at 3.37 GHz, while filter IV's TZ is located at 3.69 GHz for enhancing the stopband performance. Accordingly, the

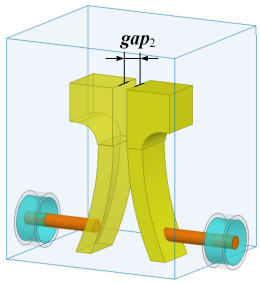

Fig. 14. Common layouts of the dual-mode-based 2nd-order filters. Dimensions (unit: mm). Filter III: $h_1 = 10.00$, $h_2 = 5.28$, $h_3 = 3.50$, $\text{gap}_1 = 9.06$, $\text{gap}_2 = 1.46$, $w_1 = 4.00$, $w_2 = 4.30$. Filter IV: $h_1 = 10.00$, $h_2 = 5.6$, $h_3 = 3.50$, $\text{gap}_1 = 10.77$, $\text{gap}_2 = 2.4$, $w_1 = 4.00$, and $w_2 = 4.30$.

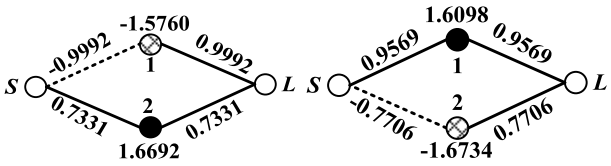

(a) (b)

Fig. 15. Topology of (a) filter III and (b) filter IV.

corresponding topology with the coupling coefficients can be given in Fig. 15(a) and (b), where the black node is CM, while the white net node denotes metal plate coupled mode. The solid line represents positive coupling, whereas the dashed line is the negative coupling to produce one TZ at either side of the passband.

In the physical realization, it has been shown in Section II that the metal plate coupled mode can exhibit the odd-mode features. This property generates opposite coupling behavior when coupled with both source and load. Specifically, in the situation where the metal plate coupled mode is the first mode and fed symmetrically, assuming that the coupling k_{s1} is negative, then k_{1L} should be positive, yielding one TZ at the lower side of the passband. Conversely, if the metal plate coupled mode is the second mode, which can be readily achieved by simply adjusting the gap_2, the TZ would be shifted to another side. For validation, the theory and EM simulated responses of both filters are plotted together for comparison, as presented in Fig. 16. The related dimensions are given in Fig. 14. As shown, the places of the desired TZs are close to the theory results, which proves the correctness of dual-mode features.

B. Four-Pole Filter Design With TZs at the Upper Stopband

By cascading two 2nd-order blocks directly, the 4th-order filter with the parallel topology can be obtained, as illustrated in Fig. 17. The blue and purple cylinders imply the electric and magnetic tuning screws, respectively. It should be noted that the post-magnetic tuning process is employed for both frequency and bandwidth tuning in this prototype since the metal plate coupled mode is also one of the resonant nodes. Also, compared with the reported works that often introduce the nonresonating node to cascade [24], [25], [26], [27], this solution achieves simple symmetrical structures and an ideal quasi-ellipse bandpass response.

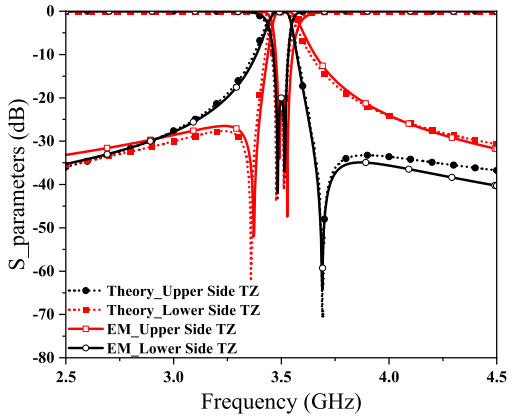

Fig. 16. Theory and EM responses of filters III and IV.

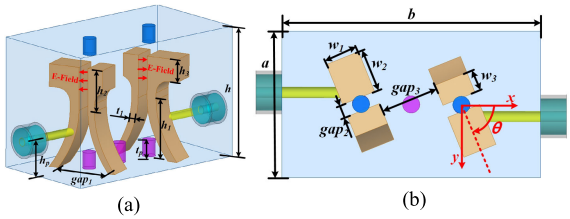

Fig. 17. Common layouts of the 4th-order dual-mode-based in-line filters. (a) Side-front view. (b) Top view. Dimensions (unit: mm). Filter V: $a = 17.00$, $b = 30.00$, $H = 20.00$, $h_1 = 9.00$, $h_2 = 7.00$, $h_3 = 3.50$, $w_1 = 4.00$, $w_2 = 5.00$, $w_3 = 3.65$, $h_p = 4.30$, $\text{gap}_1 = 4.80$, $\text{gap}_2 = 1.60$, $\text{gap}_3 = 5.39$, $t_1 = 1.5$, and $\theta = 37°$. Filter VI: $a = 17.00$, $b = 30.00$, $H = 20.00$, $h_1 = 9.20$, $h_2 = 6.60$, $h_3 = 3.50$, $w_1 = 4.00$, $w_2 = 5.00$, $w_3 = 2.50$, $h_p = 5.30$, $\text{gap}_1 = 8.38$, $\text{gap}_2 = 1.48$, $\text{gap}_3 = 7.31$, $t_1 = 1.5$, and $\theta = 62°$.

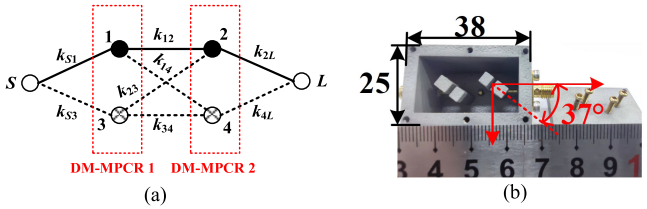

Fig. 18. (a) Topology of filter IV. (b) Printed samples of filter IV.

The designed 4th-order filter (filter V) is centered at 3.5 GHz with 25-dB RL, 200-MHz bandwidth, and two TZs located at 3.63 and 3.69 GHz. The dual parallel topology is shown in Fig. 18, where the solid and dashed lines represent the positive and negative coupling. Referring to the synthesis method in [28] and [29], the calculated $N + 2$ coupling coefficients are

$$\begin{bmatrix} 0 & 0.5153 & 0 & -1.017 & 0 & 0 \\ 0.5153 & -0.6786 & 0.2492 & 0 & -0.6615 & 0 \\ 0 & 0.2492 & -0.6786 & -0.6615 & 0 & 0.5153 \\ -1.017 & 0 & -0.6615 & 0.3612 & -1.1024 & 0 \\ 0 & -0.6615 & 0 & -1.1024 & 0.3612 & -1.017 \\ 0 & 0 & 0.5133 & 0 & -1.017 & 0 \end{bmatrix}. \quad (5)$$

In the physical implementation of the filter, the external coupling of both modes can be adjusted by controlling the height (H_p) between the ground and the feed probe. The negative coupling of k_{S3} and k_{4L} can be obtained by selecting

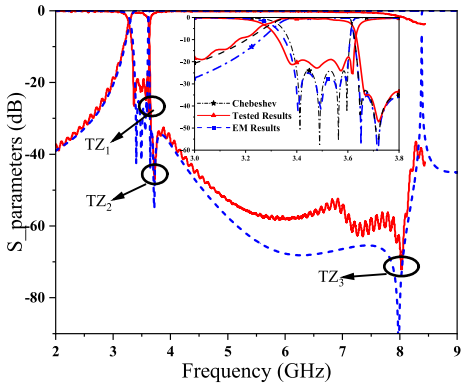

Fig. 19. Simulated and measured S-parameters of filter V.

CM as the first mode refers to the 2nd-order filter design, which is responsible for one required TZ_1 (3.63 GHz).

Hence, both gap_2 and w_1 can be used to adjust the TZ_1 places. Moreover, the distance between the adjacent DM-MPCR (gap_3) can change the coupling strength of k_{12} and k_{34}.

On the other hand, to produce the cross negative coupling between the dual modes (k_{14} and k_{23}), the metal coupled plate must be rotated as the dual modes have a pair of quasi-degenerate E-field distributions when they are parallel placed or θ is zero. Consequently, the rotation angle (θ) and the depth (t_p) of the tuning screw can control the cross-coupling strength, which is responsible for the TZ_2 as well. The critical thing is the production of the direct negative coupling of k_{34}, which is responsible for generating the TZ_2 (3.69 GHz). Usually, this negative coupling is difficult to obtain using the conventional parallel topology. Herein, it is an easy job through rotating the metal coupled plate also, which leads to the E-field directions of the two resonators being opposite, as denoted by the red arrow in Fig. 17(a).

To this end, the dimensions of filter V can be extracted with the combination of optimization in CST, which are listed in Fig. 17. The theory along with the EM simulated responses is plotted together with good agreements, as given in Fig. 19. As shown, the four-pole filter obtained ideal quasi-ellipse responses although cascading two dual-mode blocks directly, which affirms the validity of the above assumption. In detail, two anticipated TZs were observed precisely at the upper side of the passband. In addition, it deserves to be mentioned that a TZ_3 emerges at 7.96 GHz due to the mixed coupling between nodes 3 and 4, which will not be intentionally manipulated in this work. In general, filter V can provide a wide stopband from 3.6 to 8.36 GHz with rejection better than 20 dB. Moreover, the simulated IL and the average Q_u across the entire passband of the filter are 0.23 dB and 2815, respectively.

C. Four-Pole Filter Design With TZs at the Lower Stopband

On the other hand, with the same center frequency of 3.5 GHz but 30-dB RL, filter VI entails the presence of two asymmetrical TZs at 3.15 and 3.35 GHz, situated on the lower side of the passband. The filter layouts can be cross-referenced with Fig. 17. According to the above specifications, the topology of the filter can be given in Fig. 20, where the metal plate

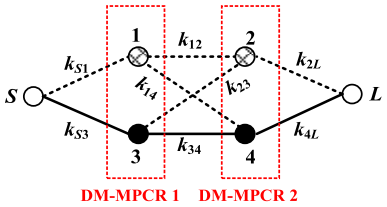

Fig. 20. Topology of filter VI.

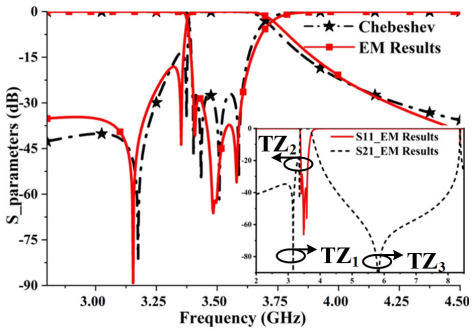

Fig. 21. Chebyshev and EM simulated responses of filter VI.

coupled mode turned into the first mode. The $N+2$ coupling coefficients are (6), as shown at the bottom of the page.

The physical realization process is the same as filter VI, except for selecting the metal plate coupled mode as the first mode. This modification can be easily achieved by adjusting the gap_2 values. Accordingly, the final dimensions can be obtained and are given in Fig. 17. The EM and theory responses are plotted together, as displayed in Fig. 21, for comparison. As presented, two expected TZs appeared at the lower stopband effectively. TZ_1 is a result of negative coupling involving k_{S1} and k_{2L}. While TZ_2 is influenced by both direct negative coupling of k_{12} and cross negative coupling of k_{12} and k_{34} simultaneously. Meanwhile, similar to filter V, the uncontrolled TZ_3 was also generated due to the mixed coupling between nodes 1 and 2. Hence, filter VI enjoys a $2.4f_0$ stopband range, featuring a rejection greater than 20 dB. Furthermore, the IL and the average Q_u are simulated at 0.30 dB and 2819, respectively.

D. Fabrication and Measurement

Filter V was chosen for manufacturing for the experimental demonstration, adopting the same 3-D printing procedure as filter II. The printed prototype of filter V is also displayed in Fig. 18(b) for size comparison, showing a half-volume size reduction compared with filter II. Specifically, the outer enclosure of the filter was divided into two pieces for printing, including one main body and one cover, which can be assembled using M2 screws. The tested mechanical tolerance in each direction was within 0.1 mm, which is acceptable for C-band applications. The measured filter responses are plotted in Fig. 19 for comparison. The noise floor is because of the limitation of the VNA. The tested f_0 and BW are 3.49 GHz and 210 MHz, respectively, which agree well with the simulated ones. The RL is -19 dB and the related IL is better than 0.58 dB. The higher loss is caused by a rough surface and relatively low conductivity of powder particles [22], while the larger BW is due to the printing tolerances. In addition, three TZs are observed in the upper stopband successfully.

In general, due to the nondegenerate dual mode features of the proposed DM-MPCR, filters V and VI fulfilled controllable TZs and quasi-ellipse bandpass responses. Both filters avoid introducing nonresonant nodes in terms of the parallel topology, which showed promising results for further research and development exploiting more advanced dual-mode coaxial resonators and filters.

V. In-Line Filter Design Based on Hybrid Modes

It is known that the "box section" scheme can be achieved by cascading two TE_{01} modes with one pair of degenerate modes ($\text{TE}_{01}/\text{TE}_{10}$), providing four poles and one controllable TZ using in-line topology as presented in [30] and [31]. To explore further design possibilities for high-rejection in-line coaxial filters, as DM-MPCR can present quasi-degenerate features, it could be assumed that cascading DM-MPCR with two single-mode coaxial resonators can also obtain similar properties. To confirm this, two filters (filters VII and VIII) with the same f_0 of 3.5 GHz, 200-MHz BW, and 20-dB RL were designed.

A. Four-Pole Filter Design With TZs at the Upper Stopband

The layouts of filter VII are given in Fig. 22, in which DM-MPCR is placed between the two outer capacitive-loaded coaxial resonators and center-rotated to the waveguide axis. The purple and blue cylinders are coupling-/frequency-tuning screws. The associated topology is given in Fig. 23(a), where S/L denotes the input–output port. Nodes 2 and 3 represent the dual modes of the DM-MPCR, with solid node 2 indicating the CM and grid-filled node 3 being the metal plate coupled mode. Furthermore, the solid line means the positive coupling, while the dashed line is the negative coupling that can produce one TZ in the upper stopband at 3.63 GHz. According to the specifications and Chebyshev filter synthesis theory [18], the required internal and external coupling coefficients can be calculated as

$$Q_{s1} = Q_{4L} = 18.0529$$
$$k_{12} = k_{24} = 0.0477; \quad k_{13} = -0.0208; \quad k_{34} = 0.0208.$$

$$\begin{bmatrix} 0 & -1.0708 & 0 & 0.5817 & 0 & 0 \\ -1.0708 & -0.4846 & -1.1999 & 0 & -0.6662 & 0 \\ 0 & -1.1999 & -0.4846 & -0.6662 & 0 & -1.0708 \\ 0.5817 & 0 & -0.6662 & 0.7976 & 0.3241 & 0 \\ 0 & -0.662 & 0 & 0.3241 & 0.7976 & 0.5817 \\ 0 & -1.0708 & -1.0708 & 0 & 0.5817 & 0 \end{bmatrix} \quad (6)$$

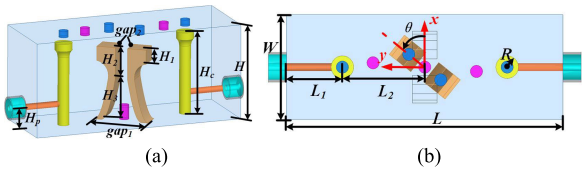

Fig. 22. (a) 3-D view of filter VII. (b) Top view of filter VII. Dimensions (unit: mm): $H_c = 17.47$, $H = 20$, $H_p = 4.5$ $H_1 = 3$, $H_2 = 6.49$, $H_3 = 9$, $\text{gap}_1 = 11.64$, $\text{gap}_2 = 2.64$, $W = 17$, $L = 45$, $L_1 = 9.07$, $L_2 = 13.43$, $R = 1.84$, and $\theta = 51.5°$.

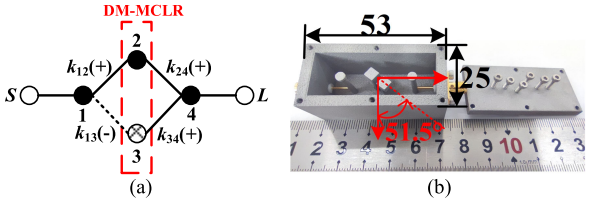

Fig. 23. (a) Topology of filter VII. (b) Printed samples of filter VII.

In the physical realization, the internal coupling (k) can be determined by adjusting L_2, which is the distance between the center of the coaxial resonator and the center of the DM-MPCR. To produce the required negative coupling path, the metal plate coupled mode needs to be selected as the first mode by adjusting the gap_2. In addition, the DM-MPCR must be rotated to allow the coupling between the CM of the outer coaxial resonators and the metal plate coupled mode, which is the same as for filter V and filter VI design. Hence, the angle (θ) can control the negative coupling strength slightly after fixing gap_2. The 50-Ω input–output coaxial cables are utilized to feed the filter. The height (H_p) between the ground and the cable can manipulate the external coupling values (Q_{s1} and Q_{4L}). To this end, the final dimensions can be extracted using the classical method described in [18] and EM full-wave simulation optimization, which are listed in Fig. 22.

The simulated filter responses along with the ideal filter are plotted together, as displayed in Fig. 24. Both results matched well, which proves the correctness of the above assumption. Compared with strongly coupled resonator in-line filters, this solution could produce an additional pole while preventing the occurrence of unwanted spurious peaks. Apart from the desired TZ, another TZ_2 was also generated that allows filter VII to have a wide stopband range with S_{12} below −50 dB from 4.0 to 8.39 GHz. The extra TZ_2 can be attributed to cross coupling between resonators 1 and 3, which explains the little deviation between S_{12} of both results at the lower stopband. It should be mentioned that we will not try to control this TZ in this filter design. Also, the maximum IL and the average Q_u at simulated are 0.2 dB and 2362, respectively.

B. Four-Pole Filter Design With a Pair of TZs

For further research to show the capability of controlling TZs, filter VIII was designed to feature a pair of TZs positions at 3.38 and 3.79 GHz. To attain this objective, filter VIII shares similar layouts to filter VII, with the exception that the DM-MCLR is parallel ($\theta = 90°$) and outer placed to the waveguide center axis, as given in Fig. 25. The parallel

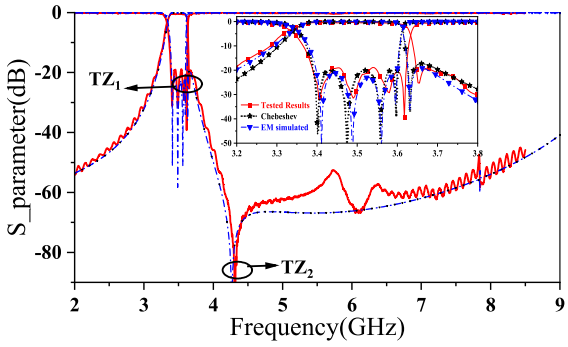

Fig. 24. Simulated and measured S-parameters of filter VII.

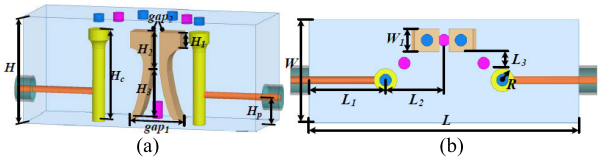

Fig. 25. (a) 3-D view of filter VIII. (b) Top view of filter VIII. Dimensions (unit: mm): $H_c = 17.47$, $H = 20$, $H_p = 4.5$, $H_1 = 3$, $H_2 = 6.49$, $H_3 = 9$, $\text{gap}_1 = 11.64$, $\text{gap}_2 = 2.64$, $W = 17$, $W_1 = 4$, $L = 45$, $L_1 = 9.07$, $R = 1.84$, $L_2 = 13.43$, and $L_3 = 3.52$.

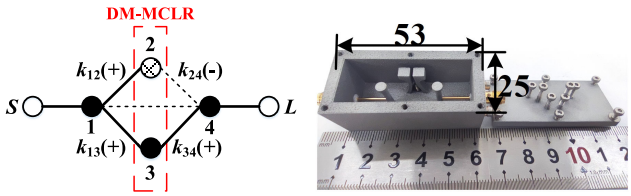

Fig. 26. (a) Topology of filter VIII. (b) Printed samples of filter VIII.

placement is for remaining physically symmetrical. The offset arrangement is to avoid the DM-MPCR blocking the cross coupling between resonators 1 and 4, which is responsible for adjusting the TZ of 3.79 GHz. The corresponding topology is shown in Fig. 26(a), where a negative coupling was introduced between nodes 1 and 4. The coupling coefficients can be given as follows:

$$Q_{s1} = Q_{4L} = 18.0560; \quad k_{12} = 0.0229$$
$$k_{24} = -0.0229; \quad k_{13} = k_{34} = 0.0411; \quad k_{14} = 0.01429.$$

The lower stopband TZ in filter VIII can be generated by choosing the metal plate coupled mode as node 2. After fixing gap_2, the required internal coupling (k_{12}, k_{13}, k_{24}, and k_{34}) can be obtained by adjusting the distances of L_1 and L_3. In addition, the distance (L_2) can manipulate the cross coupling between resonators 1 and 4 to produce the upper side TZ. For validation, Fig. 27 gives the simulated S_{21} versus different L_2 values. As can be seen, with the changing of L_2, the TZ_2 can be effectively manipulated.

Using the same design methodology as filter VII, the dimension of filter VIII can be obtained, as given in Fig. 25. The EM and measured responses are displayed in Fig. 28, which showed a consistent. Specifically, the upper TZ in filter VII was effectively shifted to the lower side of filter VIII. Moreover, a new TZ_2 was produced at the upper stopband because of the introduction of cross coupling. Therefore,

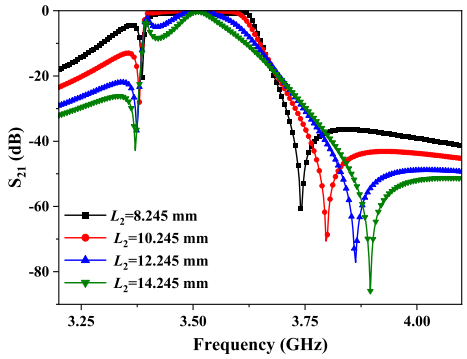

Fig. 27. Simulated S_{21} of filter VIII versus different L_2 values.

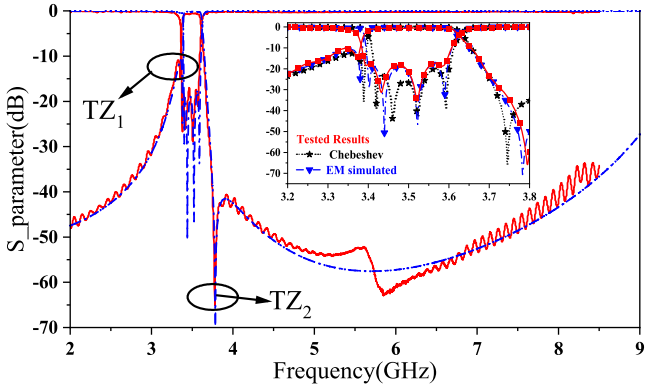

Fig. 28. Simulated and measured S-parameters of filter VIII.

filter VIII achieved a pair of controllable TZs with simple structures, leading to an excellent out-of-band rejection with S_{12} below −40 dB from 3.74 to 8.27 GHz. The simulated IL and the average Q_u are 0.2 dB and 2326, respectively.

C. Fabrication and Measurement

For experimental validation, both filters were manufactured using the same commercial 3-D metal printing technology employed in printing filters II and V. Figs. 23(b) and 26(b) give the printed samples of the two filters. The VNA (Agilent E5071C) was utilized for testing them, with the corresponding results presented in Figs. 24 and 28, respectively. The obtained testing results agreed very well with the EM results after the post-tuning process. In detail, for filter VII, the tested center frequency is 3.51 GHz within the −20-dB bandwidth from 3.39 to 3.63 GHz, and the IL performance is better than 0.61 dB throughout the passband. For filter VIII, the center frequency is 3.49 GHz within the −18-dB bandwidth from 3.39 to 3.58 GHz, and the IL is better than 0.61 dB across the passband. Hence, both filters have a 10-MHz frequency deviation and an increased IL compared to the EM simulated results, which can be attributed to the rough surface, lower conductivity of the powder particles, and inevitable printing tolerances.

To further understand the advantages of the designed filters, Table II compared filters II, V, and VIII with other reported compact in-line coaxial filters based on various technologies. The comparison includes frequencies, volumes, FBW, simulated Q_u (Sim. Q_u), and TZs. As can be observed, compared

TABLE II
COMPARED WITH OTHER PUBLISHED IN-LINE COAXIAL FILTERS

Ref	$f_{0(\mathrm{GHz})}$	FBW	Pole	Size ($\lambda\times\lambda\times\lambda$)	Sim. Q_u	TZs
[3]	2.1	2.81%	6	0.2×0.2×0.98	1425	Two
[7]	1.25	6.40%	5	0.1×0.14×0.27	1000	Two
[9]	3.85	7.8%	4	0.75×0.32×0.69	N/M	3
[21]	3.0	1.67%	4	0.75×0.54×0.54	1200	No
[32]	3.5	3.7%	6	0.18×0.19×1.05	3330	Two
Filter II	3.5	4.57%	4	0.19×0.23×0.70	2933	Three
Filter V	3.5	5.71%	4	0.19×0.23×0.35	2815	Two
Filter VIII	3.5	5.71%	4	0.19×0.23×0.52	2326	Two

N/M: Not mentioned.

with the conventional method-based in-line filters [3], [7], [9], [21], the designed filters feature much higher Q_u values with comparable volumes. Meanwhile, compared with [32], which also avoids using extra structures, filter V has comparable performance, while filters II and VIII have lower Q_u values.

VI. CONCLUSION

This article proposed a modified compact metal plate coupled resonator (MPCR), which can be designed for either single-mode or dual-mode operation in filter design. The dual mode, including one CM and one metal plate coupled mode, can be regarded as the nondegenerate modes referring to their E-field and current distributions. These properties enable the MPCR to be suitable for designing compact in-line filters having TZs for quasi-elliptical function responses based on different technologies. For the single-mode operation, the CM alone was employed to design two in-line four-pole filters, leveraging mixed-coupling technology. For the dual-mode operation, the DM-MPCR was exploited to design additional in-line four-pole filters using the principles of cross-coupling synthesis theory. Furthermore, a novel implementation of the "box section" scheme in another type of proposed filter design was achieved by cascading hybrid resonators comprised of DM-MPCR and traditional coaxial resonators. The necessity of using both electric and magnetic tuning processes for the mixed-coupling filters was first validated. In general, these designed filters all obtained compact size, high-Q_u, and controllable TZs. A 3-D printing technology was used to fabricate some prototypes for demonstration and the tested results agreed well with the simulated ones.

REFERENCES

[1] R. V. Snyder, G. Macchiarella, S. Bastioli, and C. Tomassoni, "Emerging trends in techniques and technology as applied to filter design," *IEEE J. Microw.*, vol. 1, no. 1, pp. 317–344, Jan. 2021.

[2] Y. Wang and M. Yu, "True inline cross-coupled coaxial cavity filters," *IEEE Trans. Microw. Theory Techn.*, vol. 57, no. 12, pp. 2958–2965, Dec. 2009.

[3] M. Hoft and F. Yousif, "Orthogonal coaxial cavity filters with distributed cross-coupling," *IEEE Microw. Wireless Compon. Lett.*, vol. 21, no. 10, pp. 519–521, Oct. 2011.

[4] G. Macchiarella, S. Bastioli, and R. V. Snyder, "Design of in-line filters with transmission zeros using strongly coupled resonators Pairs," *IEEE Trans. Microw. Theory Techn.*, vol. 66, no. 8, pp. 3836–3846, Aug. 2018.

[5] S. Bastioli, R. V. Snyder, and G. Macchiarella, "Design of in-line filters with strongly coupled resonator triplet," *IEEE Trans. Microw. Theory Techn.*, vol. 66, no. 12, pp. 5585–5592, Dec. 2018.

[6] Y. Zeng, Y. Yang, M. Yu, and S. Bastioli, "Synthesis of generalized strongly coupled resonator triplet filters by regulating redundant resonant modes," *IEEE Trans. Microw. Theory Techn.*, vol. 70, no. 1, pp. 864–875, Jan. 2022.

[7] S. Bastioli, R. V. Snyder, and G. Macchiarella, "The strongly coupled resonator quadruplet," *IEEE Microw. Wireless Technol. Lett.*, vol. 33, no. 8, pp. 1135–1138, Aug. 2023, doi: 10.1109/LMWT.2023.3270099.

[8] Q.-X. Chu and H. Wang, "A compact open-loop filter with mixed electric and magnetic coupling," *IEEE Trans. Microw. Theory Techn.*, vol. 56, no. 2, pp. 431–439, Feb. 2008.

[9] H. Wang and Q.-X. Chu, "An inline coaxial quasi-elliptic filter with controllable mixed electric and magnetic coupling," *IEEE Trans. Microw. Theory Techn.*, vol. 57, no. 3, pp. 667–673, Mar. 2009.

[10] S. Tamiazzo and G. Macchiarella, "Synthesis of cross-coupled filters with frequency-dependent couplings," *IEEE Trans. Microw. Theory Techn.*, vol. 65, no. 3, pp. 775–782, Mar. 2017.

[11] G. Venanzoni, M. Dionigi, C. Tomassoni, and R. Sorrentino, "3-D-printed quasi-elliptical evanescent mode filter using mixed electromagnetic coupling," *IEEE Microw. Wireless Compon. Lett.*, vol. 28, no. 6, pp. 497–499, Jun. 2018.

[12] Y. Zhang and K.-L. Wu, "A dispersive coupling structure for in-line helical resonator filters with transmission zeros," in *IEEE MTT-S Int. Microw. Symp. Dig.*, Los Angeles, GA, USA, Aug. 2020, pp. 444–447.

[13] S. Bastioli, R. V. Snyder, and P. Jojic, "High power in-line pseudoelliptic evanescent mode filter using series lumped capacitors," in *Proc. 41st Eur. Microw. Conf.*, Oct. 2011, pp. 87–90.

[14] X. Shang, J. Li, C. Guo, M. J. Lancaster, and J. Xu, "3-D printed filter based on helical resonators with variable width," in *IEEE MTT-S Int. Microw. Symp. Dig.*, Honolulu, HI, USA, Jun. 2017, pp. 1587–1590.

[15] J. J. Vague et al., "Inline combline filters of order N with up to n + 1 transmission zeros," *IEEE Trans. Microw. Theory Techn.*, vol. 69, no. 7, pp. 3287–3297, Jul. 2021.

[16] J. Rao, K. Nai, J. Marques-Hueso, P. Vaitukaitis, and J. Hong, "Inline quasi-elliptic bandpass filter based on metal 3-D printing technology," *IEEE Trans. Microw. Theory Techn.*, vol. 70, no. 4, pp. 2156–2164, Apr. 2022.

[17] J. Rao, K. Nai, P. Vaitukaitis, Y. Li, and J. Hong, "Compact 3-D metal printed filtering antenna," *IEEE Antennas Wireless Propag. Lett.*, vol. 21, no. 2, pp. 386–390, Feb. 2022.

[18] J. S. Hong and M. J. Lancaster, *Microstrip Filters for RF/Microwave Applications*. Hoboken, NJ, USA: Wiley, 2001.

[19] P. Vaitukaitis, K. Nai, J. Rao, M. S. Bakr, and J. Hong, "Technological investigation of metal 3-D printed microwave cavity filters based on different topologies and materials," *IEEE Trans. Compon., Packag., Manuf. Technol.*, vol. 12, no. 12, pp. 2027–2037, Dec. 2022.

[20] E. Lopez-Oliver et al., "3-D-printed compact bandpass filters based on conical posts," *IEEE Trans. Microw. Theory Techn.*, vol. 69, no. 1, pp. 616–628, Jan. 2021.

[21] G. Venanzoni, C. Tomassoni, M. Dionigi, M. Mongiardo, and R. Sorrentino, "Design and fabrication of 3-D printed inline coaxial filters with improved stopband," *IEEE Trans. Microw. Theory Techn.*, vol. 68, no. 7, pp. 2633–2643, Jul. 2020.

[22] R. Gumbleton, J. A. Cuenca, S. Hefford, K. Nai, and A. Porch, "Measurement technique for microwave surface resistance of additive manufactured metals," *IEEE Trans. Microw. Theory Techn.*, vol. 69, no. 1, pp. 189–197, Jan. 2021.

[23] Y. Zhang, X. Shang, F. Zhang, and J. Xu, "A 3-D printed Ku-band waveguide filter based on novel rotary coupling structure," *IEEE Microw. Wireless Technol. Lett.*, vol. 33, no. 1, pp. 35–38, Jan. 2023.

[24] J.-S. Hong, H. Shaman, and Y.-H. Chun, "Dual-mode microstrip open-loop resonators and filters," *IEEE Trans. Microw. Theory Techn.*, vol. 55, no. 8, pp. 1764–1770, Aug. 2007.

[25] Q. Liu, D. Zhou, X. Wang, M. Tang, D. Zhang, and Y. Zhang, "High-selective bandpass filters based on new dual-mode rectangular strip patch resonators," *IEEE Microw. Wireless Compon. Lett.*, vol. 31, no. 10, pp. 1123–1126, Oct. 2021.

[26] S. Bastioli and R. V. Snyder, "Nonresonating modes do it better!: Exploiting additional modes in conjunction with operating modes to design better quality filters," *IEEE Microw. Mag.*, vol. 22, no. 1, pp. 20–45, Jan. 2021.

[27] D. Miek, S. Simmich, F. Kamrath, and M. Höft, "Additive manufacturing of E-plane cut dual-mode X-band waveguide filters with mixed topologies," *IEEE Trans. Microw. Theory Techn.*, vol. 68, no. 6, pp. 2097–2107, Jun. 2020.

[28] S. Amari, "Synthesis of cross-coupled resonator filters using an analytical gradient-based optimization technique," *IEEE Trans. Microw. Theory Techn.*, vol. 48, no. 9, pp. 1559–1564, Sep. 2000.

[29] R. J. Cameron, C. M. Kudsia, and R. R. Mansour, *Microwaves Filter for Communications Systems: Fundamentals, Design and Applications*. Hoboken, NJ, USA: Wiley, 2018.

[30] U. Rosenberg and S. Amari, "Novel coupling schemes for microwave resonator filters," in *IEEE MTT-S Int. Microw. Symp. Dig.*, Seattle, WA, USA, Aug. 2022, pp. 1605–1608.

[31] M. M. Mendoza, D. Martinez, D. C. Rebenaque, and A. Alvarez-Melcon, "Enhanced topologies for the design of dual-mode filters using inductive waveguide structures," *Radio Sci.*, vol. 50, no. 1, pp. 66–77, Jan. 2015.

[32] J. Rao et al., "Analysis of the compact graded dumbbell coaxial resonator with its filter design applications," *IEEE Trans. Microw. Theory Techn.*, early access, Nov. 2, 2024, doi: 10.1109/TMTT.2023.3327474.

Jiayu Rao (Member, IEEE) received the M.Sc. degree (Hons.) in electronics science and technology from China University of Mining and Technology (CUMT), Xuzhou, China, in 2018, and the Ph.D. degree in engineering science from Heriot-Watt University (HWU), Edinburgh, U.K., in 2022.

He is currently an Associate Professor with the School of Electrical and Information Engineering, Jiangsu University of Technology (JSUT), Changzhou, China. He has authored and coauthored over 20 journal articles and conference papers in this field. His research interests include RF/microwave passive devices miniaturization and integration, such as high-Q coaxial/waveguide filters, filtering antennas, and tunable lossy filters based on 3-D metal printing, substrate integrated waveguide (SIW), and microstrip technologies.

Dr. Rao is a guest Research Fellow with the High-Tech Research Institute, Nanjing University, Changzhou.

Cong Sun received the B.Eng. degree from Suzhou University of Science and Technology, Suzhou, China, in 2021. He is currently pursuing the M.S. degree in mechanical engineering at Jiangsu University of Technology (JUST), Changzhou, China.

His current research interests include RF/microwave passive devices miniaturization and integration, such as high-Q coaxial/waveguide filters, filtering antennas, and tunable lossy filters based on 3-D metal printing and microstrip technologies.

Jiajin Lu received the B.Eng. degree from Henan University of Science and Technology, Luoyang, China, in 2016. He is currently pursuing the M.S. degree in mechanical engineering at Jiangsu University of Technology (JUST), Changzhou, China.

His current research interests include RF/microwave passive devices miniaturization and integration, such as high-Q coaxial/waveguide filters, filtering antennas, and tunable filtering antennas based on 3-D metal printing and microstrip technologies.

Qian Gao received the B.Eng. degree in applied electronic technology and the M.S. degree in engineering and electronic and communication from Nanjing University of Science and Technology, Nanjing, China, in 2002 and 2008, respectively.

She is currently a Lecturer with the School of Electric and Information Engineering, Jiangsu University of Technology (JSUT), Changzhou, China. Her current research interests include circuit and electronic technology.

Bowei Zhou received the B.Eng. degree in electrical and communication engineering from Nanjing University of Posts and Telecommunications (NJUPT), Nanjing, China, in 2013, the B.Eng. degree in computer engineering from New York Institute of Technology (NYIT), New York, NY, USA, in 2013, and the M.Sc. degree in telecommunication system management from the Northeastern University (NEU), Boston, MA, USA, in 2017.

His current research interests include RF/microwave passive device miniaturization and integration, such as high-Q coaxial/waveguide filters, tunable lossy filters based on 3-D metal printing, and microstrip technology.

Hualin Zhao received the B.Eng. degree (Hons.) in software engineering from Yangzhou University, Yangzhou, China, in 2020, and the M.Sc. degree in science of robotics from Heriot-Watt University, Edinburgh, U.K., in 2021.

Her current research interests include passive device miniaturization and integration, such as high-Q coaxial filters, tunable lossy filters based on 3-D metal printing, and microstrip technology.

Hai Liu received the B.S. and M.S. degrees in optical engineering from Huazhong University of Science and Technology, Wuhan, China, in 2003 and 2006, respectively, and the Ph.D. degree in physical electronics from Wuhan National Laboratory for Optoelectronics, Wuhan, in 2009.

He is a Professor with China University of Mining and Technology, Xuzhou, China. His current research interests include integrated optoelectronic, computational electromagnetic, and photonics.

Sheng Zhang received the Ph.D. degree in electronics science and technology from Shanghai University, Shanghai, China, in 2007.

He is currently an Associate Professor at the School of Information and Control Engineering, China University of Mining and Technology (CUMT), Xuzhou, China. He has authored or coauthored over 40 journal and conference papers in this field. His current research interests include RF/microwave integrated circuits and antennas, especially in 3-D metal printing and substrate-integrated waveguides.

Povilas Vaitukaitis (Graduate Student Member, IEEE) received the M.Eng. degree (Hons.) in mechanical engineering from the University of Aberdeen, Aberdeen, U.K., in 2019. He is currently pursuing the Ph.D. degree in electrical engineering at Heriot-Watt University, Edinburgh, U.K.

His current research interests include microwave passive device design and manufacturing using metal additive manufacturing technologies.

Mr. Vaitukaitis received the Project Award for an outstanding master's thesis project from the Institution of Mechanical Engineers (IMechE) in 2019.

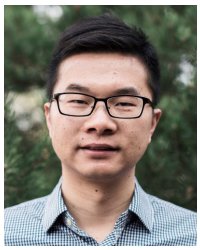

Lei Wang (Senior Member, IEEE) received the Ph.D. degree in electromagnetic field and microwave technology from Southeast University, Nanjing, China in 2015.

From 2014 to 2016, he was a Research Fellow and a Postdoctor with the Laboratory of Electromagnetics and Antennas, Swiss Federal Institute of Technology (EPFL), Lausanne, Switzerland. From 2016 to 2017, he was a Postdoctor with the Electromagnetic Engineering Laboratory, KTH Royal Institute of Technology, Stockholm, Sweden. From 2017 to 2020, he was an Alexander von Humboldt Fellow at the Institute of Electromagnetic Theory of Hamburg University of Technology, Hamburg, Germany. From 2020 to 2023, he was an Assistant Professor at the Institute of Signals, Sensors and Systems, Heriot-Watt University, Edinburgh, U.K. Since 2024, he has been an Associate Professor (Senior Lecturer) with the School of Engineering, Lancaster University, Lancaster, U.K. He has published more than 80 peer-reviewed papers and book chapters, in addition to U.K. and U.S. patents. His research interests include antenna theory and applications, active electronically scanning arrays, integrated antennas and arrays, substrate-integrated waveguide antennas, leaky-wave antennas, wireless power transfer, and wireless propagations.

Dr. Wang is the awardee of the National Ph.D. Scholarship in China in 2014, the Swiss Government Excellence Scholarship in 2014, the Alexander von Humboldt fellowship in 2016, the Principal Investigator grant from the German Research Foundation (DFG) in 2020, the British Royal Society Research Grant in 2022, and the U.K. EPSRC International Collaboration Grant in 2023. Moreover, he received the Best Poster Award in iWAT-2018, the Best Paper Award in UCET-2020, and the Best Theory and Design Antenna Paper Award in EuCAP-2023. He also supervised students winning the Honorable Mentioned Best Student Paper Award in APS-2021, the Best Student Paper Award in UCMMT-2022, the Second Place Winner in IWS-2023, and school postgraduate research prizes in 2022 and 2023.

Jiasheng Hong (Fellow, IEEE) received the D.Phil. degree in engineering science from the University of Oxford, Oxford, U.K., in 1994.

He then joined the University of Birmingham, Birmingham, U.K., until 2001 when he moved up to Edinburgh to join Heriot-Watt University, Edinburgh, U.K., and is currently a Professor leading a team for research into advanced RF/microwave device technologies. He has authored and coauthored over 200 journal articles and conference papers in this field and has published four relevant books—*Microstrip Filters for RF/Microwave Applications* (Wiley, First Edition, 2001, and Second Edition, 2011), *RF and Microwave Coupled-Line Circuits* (Artech House, Second Edition, 2007), *Balanced Microwave Filters* (Wiley, 2018), and *Advances in Planar Filters Design* (IET, 2019).

Dr. Hong is a member of the IEEE MTT Technical Committees, a Subject Editor (Microwave) of Electronics Letters, and an Associate Editor of *IET Microwaves, Antennas & Propagation*.